Journal of Colloid and Interface Science **236,** 295–304 (2001)
doi:10.1006/jcis.2000.7413, available online at http://www.idealibrary.com on IDEAL®

# Shape Factor and Hydraulic Conductance in Noncircular Capillaries

## I. One-Phase Creeping Flow

T. W. Patzek*,†,[1] and D. B. Silin†,[2]

*Department of Civil and Environmental Engineering, 591 Evans Hall, University of California, Berkeley, CA 94720; and †Lawrence Berkeley National Library, Berkeley, CA 94720

Received December 28, 2000; accepted December 29, 2000

**We use the Mason–Morrow shape factor, i.e., a dimensionless hydraulic radius, and corner half-angles to capture the geometry of noncircular capillaries pertinent to a physically adequate pore network description of porous media. We give analytic expressions for random corner half-angles that satisfy a given shape factor calculated from the microscopic images of pore space. We demonstrate that use of the shape factor leads to particularly simple expressions for the hydraulic conductance in single-phase flow through noncircular capillaries. In particular, we obtain the hydraulic conductances of arbitrary triangular ducts semianalytically, using conformal mapping. The conductances of equilateral triangular, rectangular, and elliptic ducts are calculated analytically.**



*Key Words:* **noncircular capillary; shape factor; pore network; hydraulic conductance; one-phase flow; conformal mapping.**

### 1. INTRODUCTION

The pore space of a rock is a disordered 3D network of *angular* pore bodies (sites or nodes) connected by angular pore throats (bonds or links); cf., e.g., Ref. (2). The hydraulic resistance to flow is mostly in the links. The pore throat radii are usually distributed over 2–4 orders of magnitude. Resistance to laminar flow varies as the fourth power of the smallest throat radius, and hydraulic resistance to single-fluid flow is distributed over 8–16 orders of magnitude. When two or more immiscible fluids occupy the rock, the hydraulic resistances of corner water filaments (Fig. 1), and intermediate oil filaments may span well over 20 orders of magnitude. In cases when the local hydraulic resistances are distributed over more than 4–5 orders of magnitude (3), transport is percolative, i.e., spatially heterogeneous and repeatable, rather than diffusive.

At a microscopic scale, capillary forces dominate, e.g., Refs. (2, 4). Hence, quasi-static pore network models of drainage and imbibition that fully account for capillarity can predict absolute permeability, capillary pressures, and relative permeabilities in many rocks at core scale (5–8). In fact, pore-network predictions of absolute permeability of Fontainebleau sandstone agreed with experiments over five orders of magnitude (7). Pore networks based on the three-dimensional models of rock formation and transformation processes have been especially successful in such predictions (6–8). It is therefore important to have an efficient and reliable procedure that (1) characterizes the pore angularity; (2) predicts the hydraulic conductance of angular pores in single-phase flow; and (3) predicts the hydraulic conductance of angular pores in two-phase flow with arbitrary contact angles and with a no-slip or perfect-slip boundary condition at the corner filament–bulk fluid interfaces.

This paper is organized as follows. First, we choose the Mason and Morrow shape factor to characterize the angular pores and demonstrate why this is a good choice. Second, we characterize the single-phase hydraulic conductance of noncircular capillaries in terms of this shape factor. In Part II (1) of the paper, we perform highly accurate finite element calculations and correlate the two-phase hydraulic conductance of wetting liquid in angular capillaries in terms of the corner filament shape factor, corner half-angle, and contact angle.

### 2. PORE GEOMETRY

Real pore bodies and pore throats have complex and variable cross sections. Often they are approximated as cylindrical ducts (noncircular capillaries) of constant but arbitrary cross-section. This means that the idealized pores are translationally symmetric along the cylinder generators (Fig. 2).

In pore network models, the average pore cross sections are commonly approximated by triangles of arbitrary shape, rectangles and ellipses (Fig. 3). The first two cross sections will render the simplest polygonal tubes with three and four corners. This idealization is sufficient to capture the essential geometry of real pores and the essential physics of corner flow. We do not consider here the extremely narrow slit-like pores, which should be treated as fractures.

As shown so elegantly by Hwang (9), if we know the hydraulic radius of a capillary with an arbitrary cross section, $R_h = A/P$,

[1] To whom correspondence should be addressed. E-mail: patzek@patzek.berkeley.edu. Tel: 510-643-5834.

[2] E-mail: silin@patzek.berkeley.edu.



0021-9797/01 $35.00

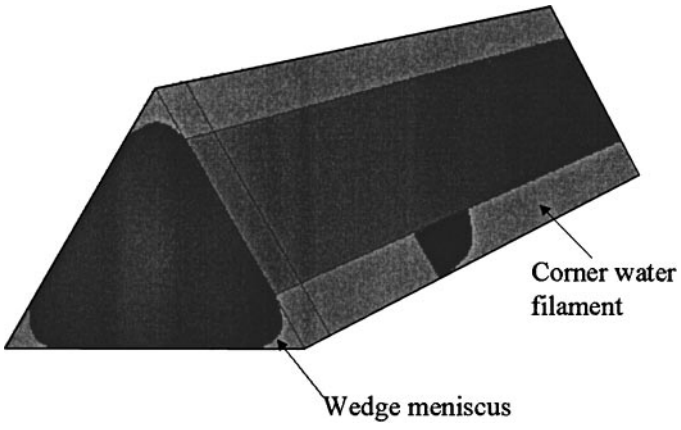


**FIG. 1.** Corner filament flow is essential; see, e.g., Ref. (2).

where $A$ is the cross-sectional area and $P$ is the perimeter, we can compute the mean curvature and the capillary rise. We can also use the hydraulic radius to vastly simplify the derivation of the Mayer–Stowe–Princen theory (10–13) of threshold capillary pressure for invasion of an angular capillary. As we shall demonstrate here, the capillary shape factor is its hydraulic radius made dimensionless by division through the perimeter.

### 2.1. Triangular Pores

We shall begin by describing the triangular capillary geometry with three independent parameters: the corner half-angles, $\beta_1$, $\beta_2$, and $\beta_3 = \pi/2 - \beta_1 - \beta_2$, and the shape factor, $G$, which can be thought of as a *dimensionless hydraulic radius* of the capillary. We adopt a convention that $0 \le \beta_1 \le \beta_2 \le \beta_3 \le \pi/2$, so that $\beta_1$ and $\beta_2$ are the two corner half-angles subtended at the longest side of the triangle (its base). The pore cross-sectional area $A$ and its perimeter $P$ can be expressed through Mason and Morrow's (14) "shape factor" defined by equation

$$G = \frac{A}{P^2} = \frac{R_h}{P} \qquad [1]$$

and the radius of the inscribed circle $r$. The pore area is

$$A = \frac{1}{2}Pr, \quad \text{or} \quad r = \frac{2A}{P} \qquad [2]$$

because the cross section is composed of six triangles of equal heights $r$, cf. Fig. 4.

**FIG. 2.** Idealization of a pore body and the attached pore throats as cylinders of square and circular cross-sections.

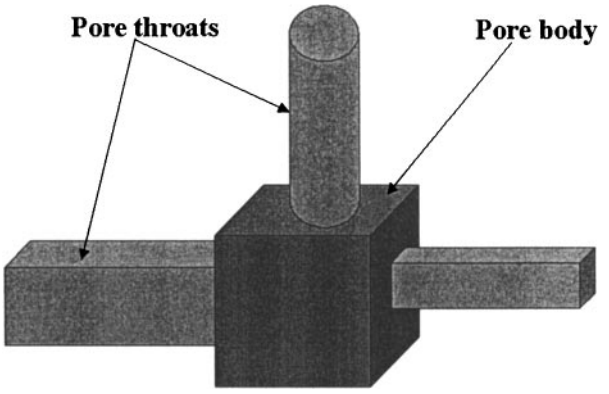


**FIG. 3.** Basic cross-sections of idealized pore bodies and pore throats.

If the radius of the inscribed circle is normalized with respect to the perimeter, then

$$\frac{r}{P} = \frac{2A}{P^2} = 2G \quad \text{or} \quad r^2 = 4GA = 4Gr^2 \sum_{i=1}^{3} \cot\beta_i. \qquad [3]$$

Hence, since $\beta_3 = \pi/2 - \beta_1 - \beta_2$,

$$G = \frac{1}{4\sum_{i=1}^{3}\cot\beta_i} = \frac{1}{4}\tan\beta_1 \tan\beta_2 \cot(\beta_1 + \beta_2). \qquad [4]$$

The maximum possible value of $G$, $G_{\max} = \sqrt{3}/36 \approx 0.048113$, corresponds to equilateral triangles with $\beta_1 = \beta_2 = \pi/6$. The minimum possible value of $G$, $G_{\min} = 0$, corresponds to slit-like pores. In Appendix A, we demonstrate that, for any admissible value of the shape factor $G$, $0 \le G \le G_{\max}$, there exist two extreme values of $\beta_2$: $\beta_{2,\min}(G)$ and $\beta_{2,\max}(G)$, beyond which Eq. [4] has no solution (see Fig. 5). More specifically, we assert the following: inasmuch as the shape factor depends only on the angles of the triangle, all possible triangles can be parameterized through all triples $(\beta_1, \beta_2, \beta_3)$ of non-negative numbers whose sum equals $\pi/2$. This parameterization becomes a one-to-one (up to a similarity) mapping if we consider only the triples sorted in the increasing order: $0 \le \beta_1 \le \beta_2 \le \beta_3 \le \pi/2$. Given a shape factor $G$, $0 \le G \le G_{\max}$, there exists an ordered triple $(\beta_1, \beta_2, \beta_3)$ of the half-angles of a triangle satisfying Eq. [4] if and only if $\beta_{2,\min}(G) \le \beta_2 \le \beta_{2,\max}(G)$, where $\beta_{2,\min}(G)$ and

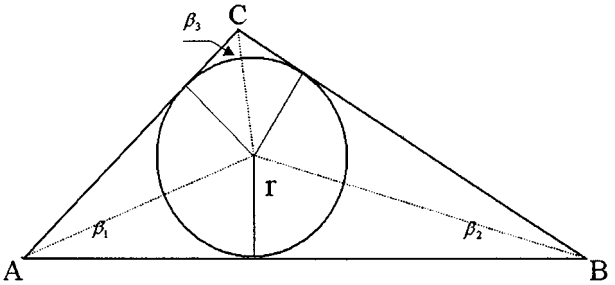


**FIG. 4.** Triangular pore cross-section.

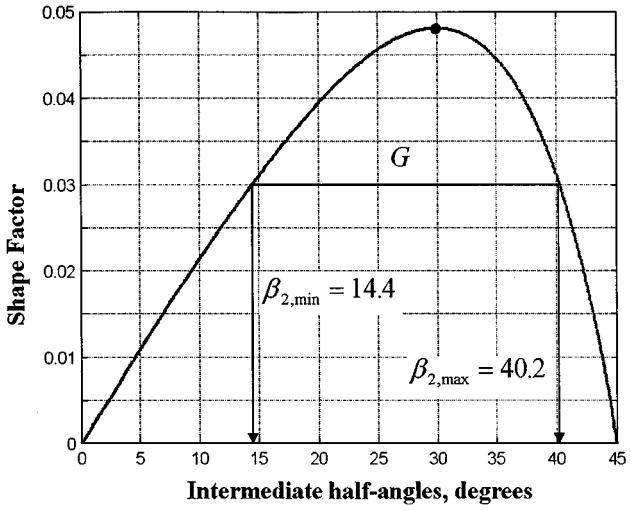


**FIG. 5.** The shape factor or "$G$-dome" for triangular pores. The feasible values of the shape factor and the base half-angles are inside the dome. The dome is parameterized by Eq. [A.9].

$\beta_{2,\max}(G)$ are calculated in Appendix A. Thus, for an admissible shape factor $G$, a triple of corner half-angles may be chosen at random as follows (Figs. 6 and 7):

(1) find the bounds on $\beta_2$, $\beta_{2,\min} \le \beta_2 \le \beta_{2,\max}$, from Eqs. [A.16] and [A.17];
(2) pick at random a value of $\beta_{2,\min} \le \beta_2 \le \beta_{2,\max}$;
(3) use Eq. [A.3] to calculate the appropriate value of $\beta_1$; and
(4) calculate $\beta_3 = \pi/2 - \beta_1 - \beta_2$.

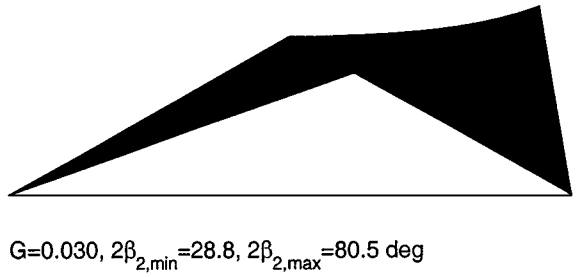


**FIG. 7.** Superimposed cross-section outlines for the 1000 realizations in Fig. 6.

### 2.2. *Rectangular and Elliptic Ducts*

For ducts with square cross sections, all four half-angles are equal to $\pi/4$ and $G = 1/16$. Circular ducts have no corners, and $G = 1/4\pi$. For simplicity, all ducts with shape factors between those of the equilateral triangle and the square can be mapped onto squares and those with shape factors above $1/16$ onto circles.

## 3. SINGLE-PHASE CREEPING FLOW IN CAPILLARY DUCTS

### 3.1. *Problem Statement*

We shall consider the steady state, creeping isothermal flow of a Newtonian, incompressible and constant viscosity fluid. With these assumptions, the continuity equation and the Navier–Stokes equation combine to produce the elliptic Poisson

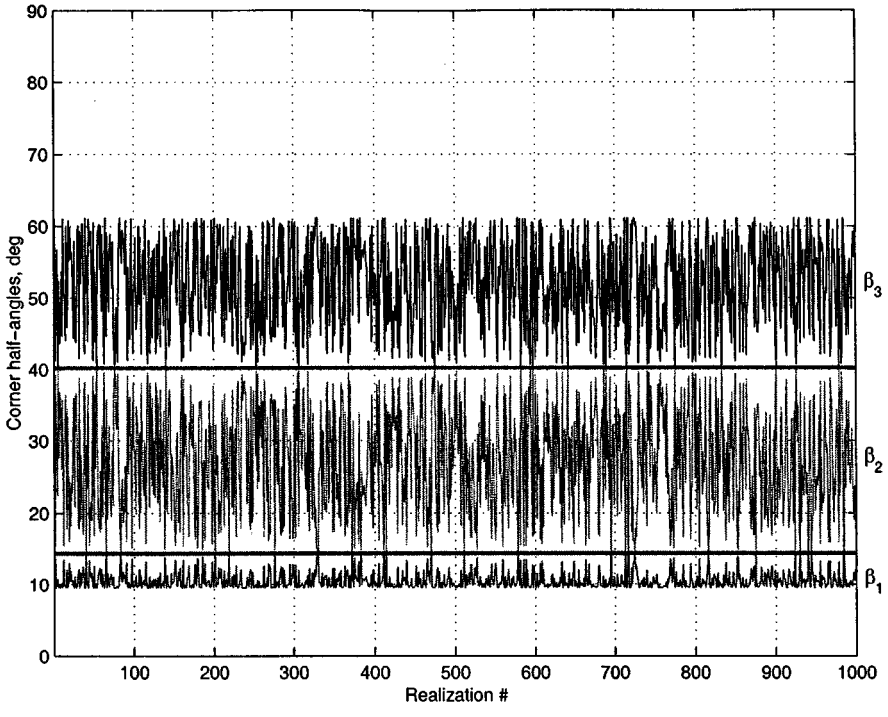


**FIG. 6.** One thousand realizations of corner half-angles for $G = 0.03$. The horizontal lines in the middle bound $\beta_2$.

equation:

$$\nabla^2 \vec{v} = \frac{1}{\mu}(\nabla p - \rho \vec{f}) \qquad [5]$$

where $\vec{v}$ is the fluid velocity, $\vec{f}$ is the body force per unit mass, $\mu$ is the fluid viscosity, and $\rho$ is its density.

We choose a Cartesian coordinate system with the $x_3$-axis parallel to the axis of the duct. We assume that within the fluid there exists a constant pressure gradient, $\partial p/\partial x_3 = -(p_0 - p_L)/L = -\Delta p/L$, in the decreasing $x_3$-direction. This pressure gradient generates a rectilinear flow field along the duct. We thus seek a solution to the following hydrodynamic problem:

$$\begin{aligned} \nabla^2 v + \frac{\Xi}{\mu} &= 0 \\ \Xi &= \left(\frac{\Delta p}{L} + \rho f_3\right) \\ v(x_1, x_2) &= 0 \text{ on } \Gamma_s, \end{aligned} \qquad [6]$$

where $\Delta p$ is the pressure drop in the duct, $L$ is the duct length, $v(x_1, x_2)$ vanishes at the duct wall $\Gamma_s$, $f_3$ is a constant, and $\Xi$ is minus the average gradient of the total driving force per unit area.

The solution of Eq. [6] allows one to relate the volumetric flow rate in the duct to the gradient of the driving force:

$$Q = \langle v \rangle A = -\boldsymbol{g}(\nabla p - \rho f_3) = \boldsymbol{g}\Xi, \qquad [7]$$

where $\langle v \rangle$ is the average flow velocity and $\boldsymbol{g}$ is the hydraulic conductance of the duct, i.e., the volumetric flow rate per unit pressure gradient. By analogy with the well-known Hagen–Poiseuille formula for cylindrical tubes, we express the flow conductance as

$$\boldsymbol{g} = \frac{r^2 A}{\chi \mu}, \qquad [8]$$

where $r$ is the inscribed circle radius, $A$ is the flow area, and $\chi$ is the dimensionless flow resistance factor,

$$\chi = \frac{r^2 \Xi}{\langle v \rangle \mu}. \qquad [9]$$

### 3.2. Hydraulic Conductance of Triangular Ducts

Let us consider a rectilinear duct with an equilateral triangle as its cross section (Fig. 8).

If we place the origin at the intersection of the medians and let the negative $x_1$-axis pass through one vertex, e.g., Ref. (15), the equation of an equilateral triangle with altitude $3a$ becomes

$$(x_1 - a)(x_1 - \sqrt{3}x_2 + 2a)(x_1 + \sqrt{3}x_2 + 2a) = 0 \qquad [10]$$

Since $\nabla^2(x_1 - a)(x_1 - \sqrt{3}x_2 + 2a)(x_1 + \sqrt{3}x_2 + 2a) = 12a$,

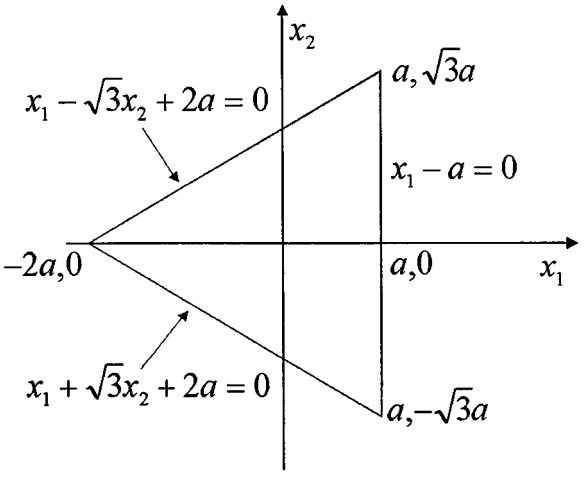


**FIG. 8.** Geometry of an equilateral triangle flow duct.

then

$$v = \left(\frac{\Xi a^2}{12\mu}\right)(1 - x_1/a)(x_1/a - \sqrt{3}x_2/a + 2) \times (x_1/a + \sqrt{3}x_2/a + 2). \qquad [11]$$

The total flow rate through the duct is obtained by integrating velocity [11] over the cross section

$$Q = \int_{x_1=-2a}^{x_1=a} \int_{x_2=-\frac{x_1+2a}{\sqrt{3}}}^{x_2=\frac{x_1+2a}{\sqrt{3}}} v(x_1, x_2)\, dy\, dx = \frac{9\sqrt{3}}{20}\frac{a^4}{\mu}\Xi \qquad [12]$$

The duct cross-sectional area is $A = 3\sqrt{3}a^2$; hence the mean velocity and volumetric flow rate are

$$\begin{aligned} \langle v \rangle &= \frac{Q}{A} = \frac{3}{20}\frac{a^2}{\mu}\Xi = \frac{1}{20\sqrt{3}}\frac{A}{\mu}\Xi \quad \text{and} \\ Q &= \boldsymbol{g}_{\max}\Xi = \frac{1}{20\sqrt{3}}\frac{A^2}{\mu}\Xi = \frac{3}{5}\frac{A^2 G_{\max}}{\mu}\Xi, \end{aligned} \qquad [13]$$

where $G_{\max} = \sqrt{3}/36$ is the equilateral triangle shape factor. Thus, the dimensionless hydraulic conductance of the equilateral triangle duct is

$$\tilde{\boldsymbol{g}}_{\max} = \frac{\boldsymbol{g}_{\max}\mu}{A^2} = \frac{3}{5}G_{\max}. \qquad [14]$$

For an arbitrary triangular duct, we shall solve the boundary-value problem [6], integrate the fluid velocity over the duct cross section, and apply Eq. [13] to calculate the hydraulic conductance as a function of the triangle shape factor. The highly accurate conformal mapping solution is described in Appendix B, and the results are shown in Fig. 9.

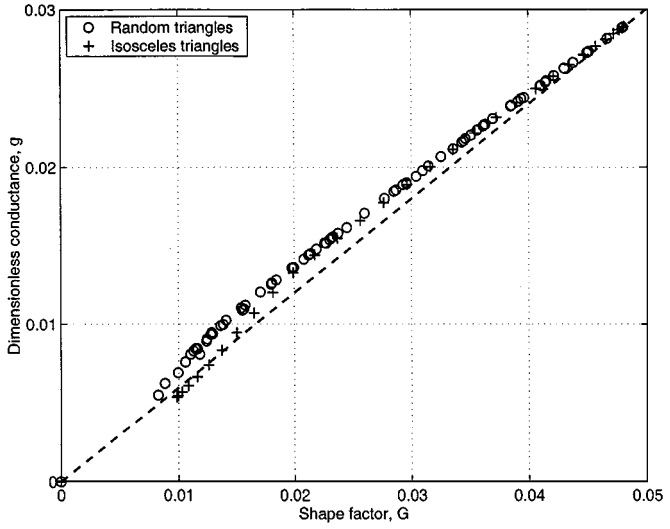


**FIG. 9.** Dimensionless hydraulic conductance versus shape factor for random and isosceles triangles from the conformal mapping solutions.

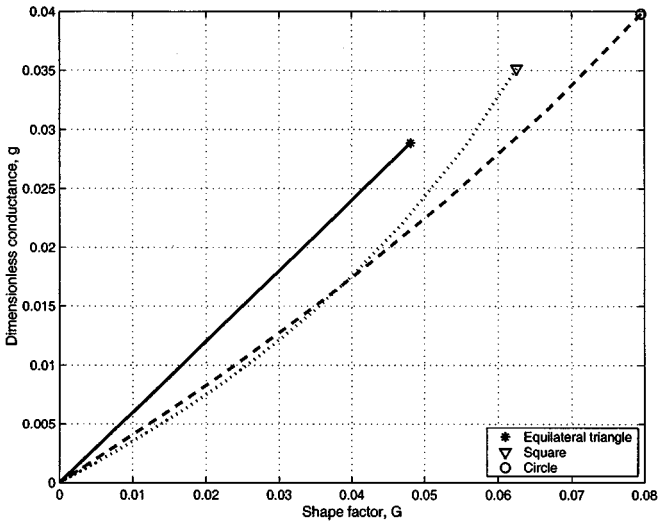


**FIG. 10.** The dimensionless hydraulic conductance vs. shape factor in one-phase flow in ducts with the triangular (solid line), rectangular (dotted line), and elliptic (dashed line) cross-sections. The shapes at the ends of the line denote the respective end-point values for equilateral triangle, square, and circle. The triangle branch approximates semi-analytical solutions; the rectangle and ellipse branches have been obtained analytically.

Figure 9 shows that the diagonal line with the slope of $3/5$ approximates the dimensionless hydraulic conductance of an arbitrary triangular cross section duct characterized by an arbitrary shape factor $G$. Thus, we assert that

$$\tilde{\boldsymbol{g}} = \frac{\boldsymbol{g}\mu}{A^2} \approx \frac{3}{5}G \qquad [15]$$

for any triangle. According to this assertion, the dimensionless conductance of a triangular duct is a straight line when plotted versus the shape factor $G$ (Fig. 10).

### 3.3. *Hydraulic Conductance of Rectangular Ducts*

If the rectangle has sides 2a and 2b, and if we choose the orientation of the coordinates system such as in Fig. 11, then the solution of Problem [6] is (15) the following:

$$v(x_1, x_2) = \frac{\Xi}{2\mu}\left[b^2 - x_2^2 + \frac{32b^2}{\pi^3} \times \sum_{n=0}^{\infty} \frac{(-1)^{n+1}\cosh[(2n+1)\pi x_1/2b]\cos[(2n+1)\pi x_2/2b]}{(2n+1)^3\cosh[(2n+1)\pi a/2b]}\right]. \qquad [16]$$

The average velocity and the hydraulic conductance are

$$\langle v\rangle = \frac{A\Xi}{4\mu\varepsilon}\left[\frac{1}{3} - \frac{64}{\varepsilon\pi^5}\sum_{n=0}^{\infty}\frac{\tanh[(2n+1)\pi\varepsilon/2]}{(2n+1)^5}\right] \quad \text{and}$$

$$\tilde{\boldsymbol{g}} = \left(1+\frac{1}{\varepsilon}\right)^2\left[\frac{1}{3} - \frac{64}{\varepsilon\pi^5}\sum_{n=0}^{\infty}\frac{\tanh[(2n+1)\pi\varepsilon/2]}{(2n+1)^5}\right]G, \qquad [17]$$

$$\varepsilon = a/b.$$

For a square duct, Eq. [17] reduces to

$$\langle v\rangle = \frac{A\Xi}{\mu}\left[\frac{1}{12} - \frac{16}{\pi^5}\sum_{n=0}^{\infty}\frac{\tanh[(2n+1)\pi/2]}{(2n+1)^5}\right] \quad \text{and}$$

$$\tilde{\boldsymbol{g}} = \left[\frac{1}{12} - \frac{16}{\pi^5}\sum_{n=0}^{\infty}\frac{\tanh[(2n+1)\pi/2]}{(2n+1)^5}\right]16G \qquad [18]$$
$$= 0.5623G.$$

The dimensionless hydraulic conductance in rectangular cross section ducts is plotted in Fig. 10 versus the shape factor.

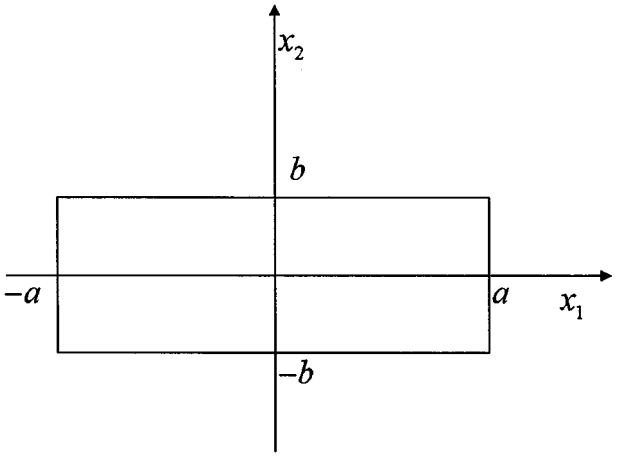


**FIG. 11.** The rectangular cross-section duct.

### 3.4. Hydraulic Conductance of Elliptic Ducts

For an elliptical cross section duct (Fig. 12), the shape factor is

$$G = \frac{\pi}{16}\frac{\varepsilon}{E^2(\sqrt{1-\varepsilon^2})},\ \varepsilon = b/a, \qquad [19]$$

where $E(e)$ is the elliptic integral of the second kind, defined as

$$E(e) = \int_0^1 \sqrt{\frac{1-e^2t^2}{1-t^2}}\,dt = \int_0^{\pi/2} \sqrt{1-e\sin^2 t}\,dt, \qquad [20]$$

where

$$e \equiv \frac{c}{a} = \frac{\sqrt{a^2-b^2}}{a} = \sqrt{1-\varepsilon^2} \qquad [21]$$

is the ellipse eccentricity. For a circle, $e = 0$, $E(0) = \pi/2$, and $G = 1/(4\pi)$.

The dimensionless hydraulic conductance of an elliptical duct is

$$\tilde{g} = \frac{1}{4\pi}\frac{\varepsilon}{1+\varepsilon^2} = \frac{4}{\pi^2}\frac{E^2(\sqrt{1-\varepsilon^2})}{1+\varepsilon^2}G. \qquad [22]$$

If one approximates the circumference of the ellipse as

$$P \approx 2\pi\sqrt{\frac{a^2+b^2}{2}}, \qquad [23]$$

then

$$G = \frac{A}{P^2} \approx \frac{\pi ab}{2\pi^2(a^2+b^2)} = \frac{1}{2\pi}\frac{\varepsilon}{1+\varepsilon^2}, \qquad [24]$$

and Eq. [22] can be approximated as

$$\tilde{g} \approx \frac{1}{2}G. \qquad [25]$$

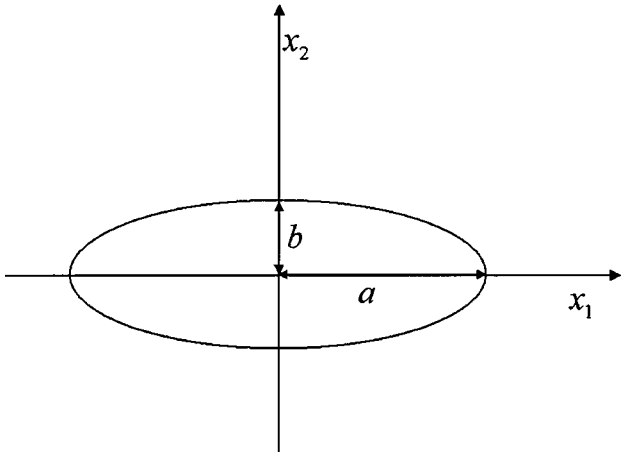


**FIG. 12.** The elliptic cross-section duct.

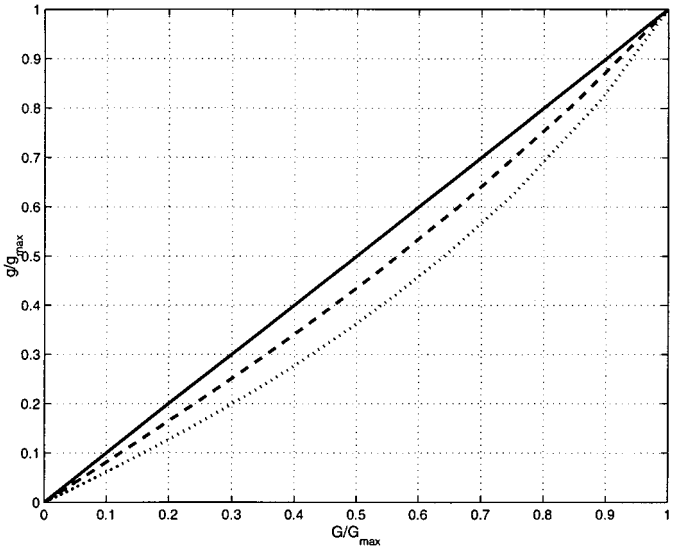


**FIG. 13.** The rescaled hydraulic conductances vs. rescaled shape factors for the rectangular (dotted line), elliptic (dashed line), and triangular (solid line) cross-section ducts.

Expression [23] approximates the exact ellipse circumference to within 11%. For the circular cross section duct, of course, the well-known (16) result is exact equality in Eq. [25].

The shape factors and the dimensionless conductances may be scaled from zero to one by division through the respective end-point values. The rescaled conductances may then be fit with polynomials, Fig. 13.

Rectangle: $g = 0.3214\mathcal{G}^3 + 0.0630\mathcal{G}^2 + 0.6109\mathcal{G}$, where

$$\mathcal{G} = \frac{G}{G_{\max}} = 16G \quad \text{and} \quad g = \frac{\tilde{g}}{\tilde{g}_{\max}} = \frac{\tilde{g}}{0.5623/16} \qquad [26]$$

Ellipse: $g = 0.1366\mathcal{G}^3 + 0.0556\mathcal{G}^2 + 0.8077\mathcal{G}$, where

$$\mathcal{G} = \frac{G}{G_{\max}} = 4\pi G \quad \text{and} \quad g = \frac{\tilde{g}}{\tilde{g}_{\max}} = \frac{\tilde{g}}{1/(8\pi)} \qquad [27]$$

## 4. CONCLUSIONS

1. The geometric significance of the Mason and Morrow shape factor has been elucidated for the triangular cross section capillaries, and an analytic algorithm for calculating the admissible capillary shapes, given the shape factor, has been described.

2. The shape factor plays an important role in obtaining the semi-analytical or analytical expressions for the hydraulic conductances of noncircular capillaries filled with a single fluid.

3. In particular, the dimensionless hydraulic conductances of triangular, rectangular, and elliptic ducts filled with a single fluid are simple power functions of the shape factor.

## APPENDIX A

### Admissible Shape Factor and Half-Angles

To investigate the solvability of Eq. [4], let us rewrite it in the following equivalent form

$$G = \frac{1}{4}\tan\beta_2\left(1 - \frac{2}{1+\frac{\sin(2\beta_1+\beta_2)}{\sin\beta_2}}\right). \qquad [A.1]$$

Since $\beta_1 \le \beta_2 \le \beta_3$ and $\beta_1+\beta_2+\beta_3 = \frac{\pi}{2}$ we infer that

$$0 \le \beta_1 \le \frac{\pi}{6} \quad \text{and} \quad \beta_1 \le \beta_2 \le \frac{\pi}{4} - \frac{\beta_1}{2}. \qquad [A.2]$$

Equation [A.1] (and, therefore, Eq. [4]) can be solved with respect to $\beta_1$ explicitly:

$$\beta_1 = -\frac{1}{2}\beta_2 + \frac{1}{2}\arcsin\left(\frac{\tan\beta_2 + 4G}{\tan\beta_2 - 4G}\sin\beta_2\right). \qquad [A.3]$$

From Eq. [A.2] and with $\beta_3 = \frac{\pi}{2} - (\beta_1+\beta_2)$ we immediately obtain that

$$\frac{\pi}{4} - \frac{\beta_1}{2} \le \beta_3 \le \frac{\pi}{2} - \beta_1. \qquad [A.4]$$

Comparing Eqs. [A.2] and [A.4] we automatically get $\beta_2 \le \beta_3$; therefore, all three of the half-angles are ordered in ascending order. Hence, both $0 \le \beta_1 \le \beta_2 \le \beta_3$ and $\beta_1+\beta_2+\beta_3 = \frac{\pi}{2}$ hold true simultaneously if and only if the inequalities [A.2] hold true. Inequalities [A.2] can be equivalently rewritten in the following form:

$$0 \le \beta_2 \le \frac{\pi}{4} \quad \text{and} \quad 0 \le \beta_1 \le \begin{cases} \beta_2, & \text{if } 0 \le \beta_2 \le \dfrac{\pi}{6} \\ \dfrac{\pi}{2} - 2\beta_2, & \text{if } \dfrac{\pi}{6} < \beta_2 \le \dfrac{\pi}{4} \end{cases}. \qquad [A.5]$$

Now, if we fix the half angle, $\beta_2$, the unconstrained maximum of the right-hand side of Eq. [A.1] with respect to $\beta_1$ is attained at $\beta_1 = \frac{\pi}{4} - \frac{\beta_2}{2}$. As $\beta_1$ increases from 0 to this value, the right-hand side of Eq. [A.1] (and of Eq. [4]) also increases monotonically. However, the angle $\beta_1$ is restricted by inequalities [A.5], and a straightforward calculation demonstrates that the inequality $\beta_2 \le \frac{\pi}{4} - \frac{\beta_2}{2}$ holds true if $0 \le \beta_2 \le \frac{\pi}{6}$, and $\frac{\pi}{2} - 2\beta_2 \le \frac{\pi}{4} - \frac{\beta_2}{2}$ holds true if $\frac{\pi}{6} < \beta_2 \le \frac{\pi}{4}$. Therefore, the constrained maximum of the right-hand side of Eq. [A.1] with respect to $\beta_1$ is attained at

$$\beta_1(\beta_2) = \begin{cases} \beta_2, & \text{if } 0 \le \beta_2 \le \dfrac{\pi}{6} \\ \dfrac{\pi}{2} - 2\beta_2, & \text{if } \dfrac{\pi}{6} < \beta_2 \le \dfrac{\pi}{4} \end{cases}. \qquad [A.6]$$

Obviously, from $\beta_1 = \frac{\pi}{2} - 2\beta_2$ it follows that $\beta_2 = \beta_3$. Since permutation of the angles in a triangle does not affect its shape factor, we can flip $\beta_1$ with $\beta_3$ when $\frac{\pi}{6} < \beta_2 \le \frac{\pi}{4}$. Such a transformation simplifies Eq. [A.6] into

$$\beta_1(\beta_2) = \beta_2, \quad 0 \le \beta_2 \le \frac{\pi}{4}. \qquad [A.7]$$

Therefore, to plot all admissible shape factors versus $\beta_2$ we just need to substitute Eq. [A.7] into Eq. [A.1]:

$$G_{\max}(\beta_2) = \frac{1}{4}\tan\beta_2\left(1 - \frac{2}{1+\frac{\sin(3\beta_2)}{\sin\beta_2}}\right), \quad 0 \le \beta_2 \le \frac{\pi}{4}. \qquad [A.8]$$

By using standard trigonometric identities, we reduce Eq. [A.8] to

$$G_{\max}(\beta_2) = \frac{-\tan^3\beta_2 + \tan\beta_2}{8}. \qquad [A.9]$$

The plot of the function defined by Eq. [A.9] gives us the shape of the dome in Fig. 5. To find the limits $\beta_{2,\min}$ and $\beta_{2,\max}$ for a given admissible shape factor $G$, we need to investigate the solution to the cubic equation

$$t^3 - t + 8G = 0 \qquad [A.10]$$

with $G$ between 0 and $G_{\max} = \sqrt{3}/36$. Since $t = \tan(\beta_2)$ and $\beta_2$ varies between 0 and $\pi/4$, we are looking only for the solutions to Eq. [A.10] that are between 0 and 1. If $G = 0$, Eq. [A.10] has two roots fulfilling this condition $t = 0$ and $t = 1$ (see Fig. 14a) that corresponds to $\beta_2 = 0$ and $\beta_2 = \frac{\pi}{4}$. When $G = G_{\max} = \sqrt{3}/36$, Eq. [A.10] admits only one double root $t = 1/\sqrt{3}$ in the interval [0, 1] (respectively, $\beta_2 = \frac{\pi}{6}$, an equilateral triangle) (Fig. 14c). In an intermediate case, where $0 < G < \sqrt{3}/36$ (Fig. 14b), we obtain two roots $0 < t_{\min} < t_{\max} < 1$. Therefore, we obtain

$$\beta_{2,\min} = \arctan(t_{\min}) \quad \text{and} \quad \beta_{2,\max} = \arctan(t_{\max}). \qquad [A.11]$$

To calculate $t_{\min}$ and $t_{\max}$ analytically, we apply the Cardano formulae. We obtain for all the roots of Eq. [A.10]

$$t_{1,2,3} = \frac{2}{\sqrt{3}}Re\sqrt[3]{-12\sqrt{3}G + i\sqrt{1-432G^2}} \qquad [A.12]$$

where $i$ is the imaginary unit. To select the two non-negative solutions out of the three given by Eq. [A.12], we apply the following argument. Clearly, all solutions are represented by

$$t_v = \frac{2}{\sqrt{3}}\cos\left(\frac{\varphi_v}{3}\right), \quad \text{where}$$

$$\varphi_v = \arccos(-12\sqrt{3}G) + 2\pi(v-1) \text{ and } v = 1, 2, 3. \qquad [A.13]$$

Moreover, Eq. [A.13] implies that $\frac{\pi}{2} \le \varphi_1 \le \pi$. Hence $\frac{\pi}{6} \le$

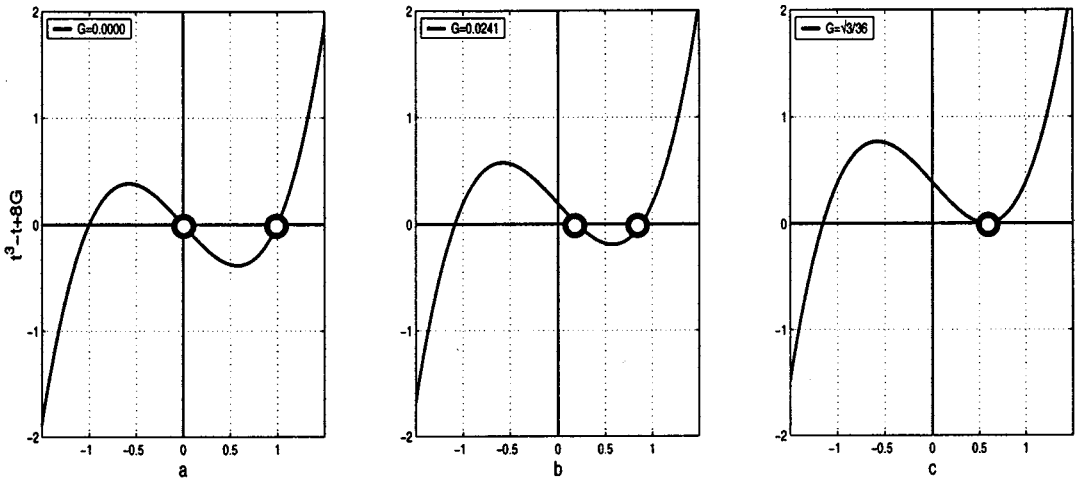


**FIG. 14.** Plot of the cubic polynomial [A.10] at different values of $G$: $G = 0$ (a); $G = 0.0241$ (b); and $G = G_{\max}$ (c).

$\frac{\varphi_1}{3} \leq \frac{\pi}{3}$, and the roots [A.12] are located as shown in Fig. 15. Hence,

$$t_{\min} = t_3 = \frac{2}{\sqrt{3}} \cos\left(\frac{\arccos(-12\sqrt{3}G)}{3} + \frac{4\pi}{3}\right) \qquad [A.14]$$

and

$$t_{\max} = t_1 = \frac{2}{\sqrt{3}} \cos\left(\frac{\arccos(-12\sqrt{3}G)}{3}\right). \qquad [A.15]$$

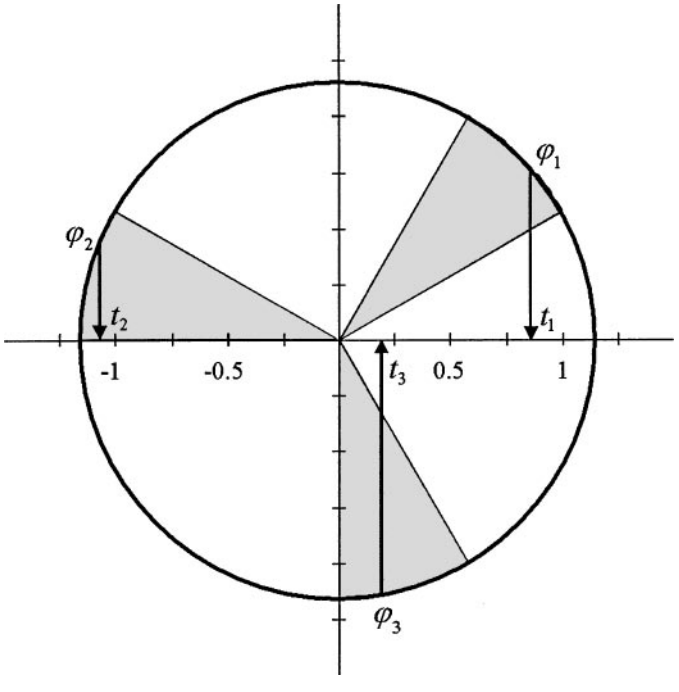


**FIG. 15.** Locations of the angles $\varphi_{1,2,3}$ and the roots $t_{1,2,3}$.

Thus, finally we obtain:

$$\beta_{2,\min} = \arctan\left(\frac{2}{\sqrt{3}} \cos\left(\frac{\arccos(-12\sqrt{3}G)}{3} + \frac{4\pi}{3}\right)\right) \qquad [A.16]$$

and

$$\beta_{2,\max} = \arctan\left(\frac{2}{\sqrt{3}} \cos\left(\frac{\arccos(-12\sqrt{3}G)}{3}\right)\right). \qquad [A.17]$$

## APPENDIX B

### Solution of a Triangular Duct Flow Problem using Conformal Mapping

The boundary value problem [6] for a Poisson equation in a triangle can be solved semi-analytically using conformal mapping techniques; see Ref. (17). To do this, we need to complete three steps. First, a conformal mapping of the unit disk onto the triangular domain where we are solving the boundary value problems should be constructed. Second, we need to impose boundary conditions in such a way that we obtain a Dirichlet problem for a Laplace equation, which is equivalent to the original problem. We then calculate the image of the boundary conditions on the unit circle where the conformal mapping is applied. In the unit disk the solution to the Laplace equation is calculated from Poisson's integral. In the third step, the solution in the original domain is obtained from the solution on the unit disk with the conformal mapping constructed above, and finally, the solution to the original Poisson equation (Eq. [6]) is calculated. In this appendix, we describe in more detail how this procedure works in our case.

A conformal mapping of a unit disk onto a triangle with the angles $2\beta_1$, $2\beta_2$, and $2\beta_3$ (Fig. 4) is given by

$$w = S(z) = C_1 \int_{z_0}^{z} (\zeta - \zeta_1)^{\alpha_1}(\zeta - \zeta_2)^{\alpha_2}(\zeta - \zeta_3)^{\alpha_3}\, d\zeta + C_2. \qquad [B.1]$$

Here $C_1$ and $C_2$ are complex coefficients which define rotation, dilation, and shift in the plane $w$, the exponents $\alpha_i$ are determined by the angles of the triangle $\alpha_i = \frac{\beta_i}{\pi} - 1$, and $\zeta_i$ are arbitrary complex numbers whose modules are equal to one, $i = 1, 2, 3$. The complex number $z_0$ also can be chosen arbitrarily inside the unit disk. The arbitrariness, however, assumes that the coefficients $C_1$ and $C_2$ have to be recalculated as a different set of parameters $\zeta_i$ and $z_0$ is selected. The choice of the parameters $\zeta_i$ also determines the point onto which the center of the disk is mapped.

Numerical algorithms for computing the parameters for the transformation defined by Eq. [B.1] have been developed recently (18) and are available both in Fortran and in MATLAB[3] versions (19, 20).

To apply transformation [B.1], we need to slightly modify the boundary-value problem (Eq. [6]). For this purpose we will look for the solution to Eq. [6] in the form

$$v(x_1, x_2) = v_0(x_1, x_2) + u(x_1, x_2), \qquad [B.2]$$

where $v_0(x_1, x_2)$ is a function satisfying the Poisson equation, but probably violating the boundary conditions, whereas the function $u(x_1, x_2)$ satisfies Laplace equation with some boundary conditions in such a way that the sum [B.2] is the solution to Eq. [6]. There is a certain arbitrariness in the choice of $v_0(x_1, x_2)$, but for simplicity we put

$$v_0(x_1, x_2) = -\frac{\Xi}{4\mu}(x_1 + x_2)^2. \qquad [B.3]$$

Then, for the function $u(x_1, x_2)$ we obtain the following boundary-value problem:

$$\nabla^2 u(x_1, x_2) = 0,$$
$$u(x_1, x_2)|_\Gamma = \frac{\Xi}{4\mu}(x_1 + x_2)^2. \qquad [B.4]$$

If we introduce a complex variable $w = x_1 + x_2 i$, then from [B.1]

$$\varphi(\eta_1, \eta_2) = u(\mathrm{Re}\ S(z), \mathrm{Im}\ S(z)), \qquad [B.5]$$

where $z = \eta_1 + \eta_2 i$ is a harmonic function defined on the unit disk. A conformal transformation [B.1] maps the unit circle onto the boundary of the triangle $\Gamma$; therefore the boundary condition for the function $\varphi$ is

$$\varphi(\eta_1, \eta_2)|_{\eta_1^2 + \eta_2^2 = 1} = \frac{\Xi}{4\mu}(\mathrm{Re}\ S(\eta_1 + i\eta_2) + \mathrm{Im}\ S(\eta_1 + i\eta_2))^2. \qquad [B.6]$$

The solution to the Laplace equation with the boundary condition

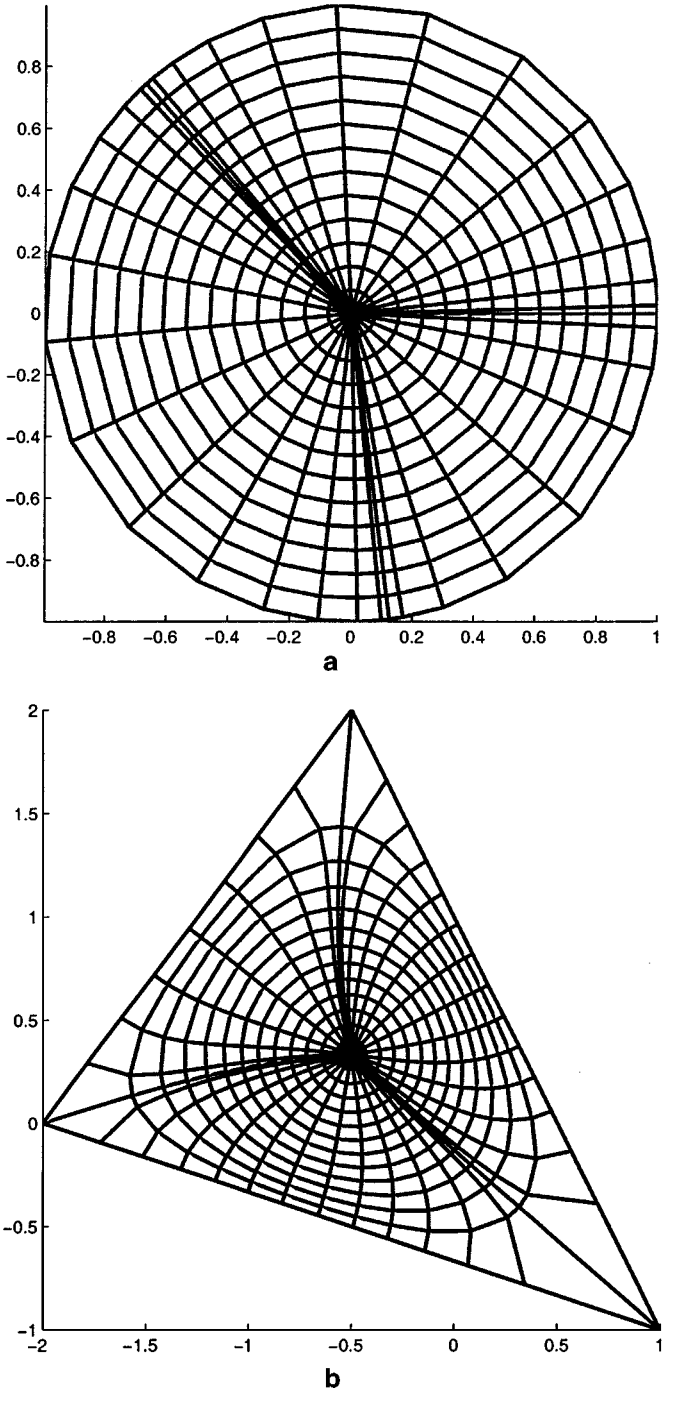


**FIG. 16.** An example of conformal mapping of the unit disk onto a triangle. The polar grid (a) is transformed into a curvilinear grid (b) in the triangle.

[3] MATLAB is a registered trademark of MathWorks, Inc.

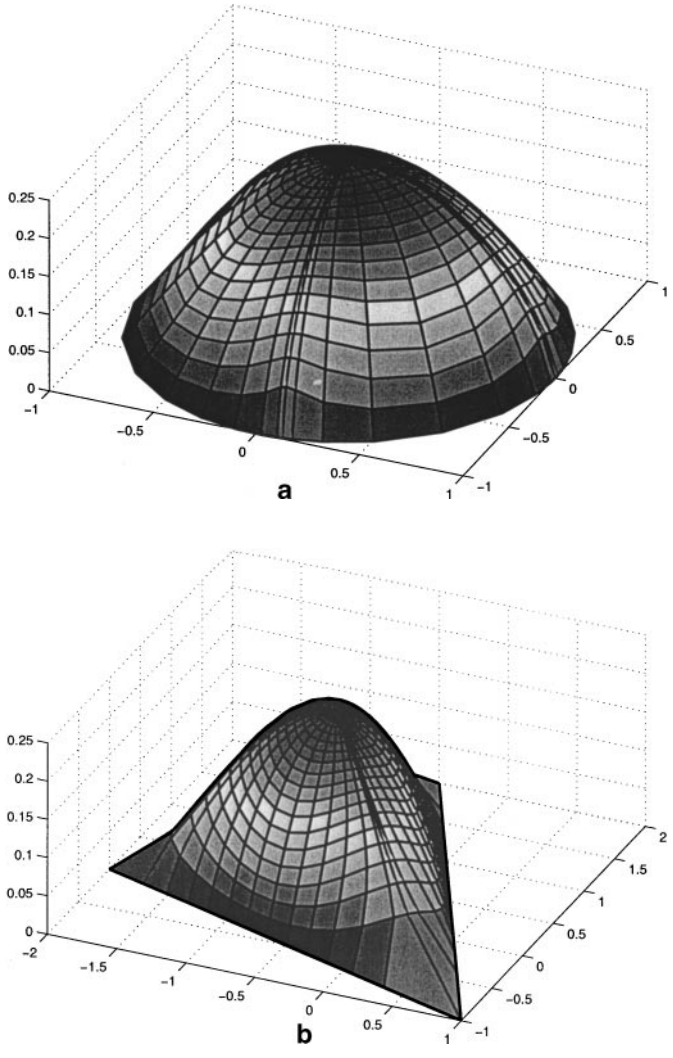


**FIG. 17.** (a) The fluid velocity obtained on the unit disk, and (b) its image after mapping [B.1].

defined by Eq. [B.6] is furnished by the Poisson integral (17):

$$\varphi(\eta_1, \eta_2) = \frac{1}{2\pi} \int_{-\pi}^{\pi} \frac{\Xi}{4\mu} |S(z(\alpha))|^2 \frac{1-\rho^2}{\rho^2 - 2\rho\cos(\alpha - \psi) + 1}\, d\alpha, \qquad [B.7]$$

where $|S(z(\alpha))|^2 = (\mathrm{Re}\ S(\cos\alpha + i\sin\alpha) + \mathrm{Im}\ S(\cos\alpha + i\sin\alpha))^2$, $\rho = (\eta_1^2 + \eta_2^2)^{1/2}$, and $\psi$ is an argument of $z = \eta_1 + \eta_2 i$, i.e., $z = \rho e^{i\psi}$. Putting Eqs. [B.2], [B.3], [B.5], and [B.7] together, we obtain the solution to the original boundary-value problem (Eq. [6]).

Practically, the following scheme can be applied. First, a set of Schwarz–Christoffel transformation parameters is selected. Second, we set up a grid on the unit circle to evaluate the Poisson integral [B.7]. Since the integrand can be evaluated at an arbitrary point, we apply a higher-order Gaussian quadrature scheme. It is desirable, however, that the original pre-images of the vertices of the triangle are the endpoints of some integration subintervals, rather than interior points. As soon as the quadrature nodes and the coefficients are calculated, the solution (Eq. [B.7]) can be computed at any point inside the unit disk, which then can be mapped onto the triangle. Examples of a grid in the unit disk and the image of this grid in the triangle are presented in Fig. 16. A grid in polar coordinates in the unit disk generates a curvilinear grid in the triangle. Note that we generated a grid condensing around the original pre-images of the vertices (Fig. 16a) to make the grid in the triangle more evenly spaced near the vertices (Fig. 16b).

An example of computation of the solution using the transformation [B.1] is presented in Fig. 17. In Fig. 17a, the original pre-image solution in the unit disk is displayed. In Fig. 17b, we show the solution of Eq. [6] on the triangular domain evaluated at the nodes of the curvilinear grid shown in Fig. 16.

## ACKNOWLEDGMENTS

This work was partially supported by the U.S. Department of Energy under Contract DE-AC03-76SF00098 and by a gift from Statoil to the UC Oil Consortium at the University of California at Berkeley.

## REFERENCES

1. Patzek, T. W., and Kristensen, J. G., *J. Colloid Interface Sci.* **236,** 30 (2001) dol:10.1006/jcis.2000.7414.
2. Patzek, T. W., "E240—Fundamentals of Multiphase Flow in Porous Media," First ed., p. 250, U.C. Berkeley, Berkeley, CA 1999.
3. Kirkpatrick, S., *in* "5th Annual Conference on Amorphous and Liquid Semiconductors: Proceedings," Taylor & Francis, London, 1973.
4. Hilfer, R., and Øren, P. E., *Transp. Porous Media* **22,** 53 (1996).
5. Blunt, M. J., and Sher, H., *Phys. Rev. E* **52,** 6387 (1995).
6. Lerdhal, T. R., and Oren, P. E., *in* "SPE/DOE Improved Oil Recovery Symposium, Tulsa, OK, 2000," SPE 59311.
7. Øren, P.-E., Bakke, S., and Arntzen, O. J., *Soc. Pet. Eng. J.* **3**(4), 324 (1998).
8. Patzek, T. W., SPE 59312, *in* "SPE/DOE Improved Oil Recovery Symposium, Tulsa, OK, 2000," SPE 59312 (in print JPEJ).
9. Hwang, S.-T., *Z. Phys. Chem. N. F.* **105,** 225 (1977).
10. Mayer, R. P., and Stowe, R. A., *J. Colloid Interface Sci.* **30,** 893 (1965).
11. Princen, H. M., *J. Colloid Interface Sci.* **30,** 60 (1969).
12. Princen, H. M., *J. Colloid Interface Sci.* **30,** 359 (1969).
13. Princen, H. M., *J. Colloid Interface Sci.* **34,** 171 (1970).
14. Mason, G., and Morrow, N. R., *J. Colloid Interface Sci.* **141,** 262 (1991).
15. Langlois, W. E., "Slow Viscous Flow," The Macmillan Company, New York, 1964.
16. Bird, R. B., Stewart, W. E., and Lightfoot, E. N., *in* "Transport Phenomena," Wiley, New York, 1960.
17. Tikhonov, A. N., and Samarskii, A. A., "Equations of mathematical physics," International Series of Monographs in Pure and Applied Mathematics, vol. 39, Macmillan, New York, 1963.
18. Treefethen, L. N., *SIAM J. Sci. Stat. Comput.* **1**(1), 82 (1980).
19. Treefethen, L. N., "SPACK User's Guide," MIT Numerical Analysis Report 89-2. 1989.
20. Driscoll, T. A., *Schwarz–Christoffel Toolbox, Version 2.1*. 1998.